A 0.85 mm^2 51%-Efficient 11-dBm Compact DCO-DPA in 16-nm FinFET for Sub-Gigahertz IoT TX Using HD$_2$ Self-Suppression and Pulling Mitigation

Kai Xu, *Student Member, IEEE*, Feng-Wei Kuo, Huan-Neng Ron Chen, Lan-Chou Cho, Chewn-Pu Jou, Mark Chen, and Robert Bogdan Staszewski, *Fellow, IEEE*

***Abstract*—In this paper, we propose a sub-gigahertz transmitter (TX) with a physically merged digitally controlled oscillator (DCO) and digital power amplifier (DPA). The matching transformer of single-ended DPA is placed inside the DCO transformer to save ∼50% of area. The resulting DCO pulling is compensated via a feedback path and an inter-winding cancellation capacitor suppresses the second harmonic. Fabricated in 16-nm FinFET CMOS, the DPA reaches 51% efficiency at 11-dBm output with < −55-dBc HD$_2$. The 1.8-GHz DCO exhibits −116-dBc/Hz phase noise (PN) at 1-MHz offset and draws 195 uW from 0.3-V supply. The error vector magnitude measured with a 2-MHz 64-Quadratic amplitude modulation (QAM) orthogonal frequency division multiplexing signal at 5-dBm average power is 3.7%.**

***Index Terms*—802.11ah, digital power amplifier (DPA), harmonic suppression, Internet-of-Things (IoT), interwinding capacitance, pulling mitigation, RF oscillator, sub-gigahertz, transformer, transmitter (TX).**

I. Introduction

IEEE 802.11ah aims to facilitate ultralow-power (ULP) and low-cost wireless connectivity in the 900-MHz band. It is indispensable for a number of Internet-of-Things (IoT) applications, such as Smart Home and Smart City, where the coverage range of IoT devices is more important than the data throughput. Furthermore, it is less prone to interference compared to the more popular standards, such as Wi-Fi, Bluetooth, and ZigBee, in the crowded 2.4-GHz band. Unfortunately, the relatively low sub-gigahertz band makes it very difficult to inexpensively integrate RF passive components, especially inductors or transformers utilized for frequency generation or impedance matching, in a way it has been successfully done at 2.4 GHz [1]–[3]. For the sake of frequency tuning and frequency selection in the sub-gigahertz band, a larger inductor is preferred in a parallel inductor–capacitor (LC) resonant tank to maintain a reasonable tank quality factor Q_T, which is dominated by the inductor's Q_L. The larger inductor requires a larger radius r, inevitably increasing the size and thus ultimately the cost, which is rather against the low-cost philosophy of IoT. In this paper, we attempt to address it by proposing a highly compact fully integrated digital RF front end, i.e., a digitally controlled oscillator (DCO) and an 8-bit digital power amplifier (DPA), of a 900-MHz band transmitter (TX).

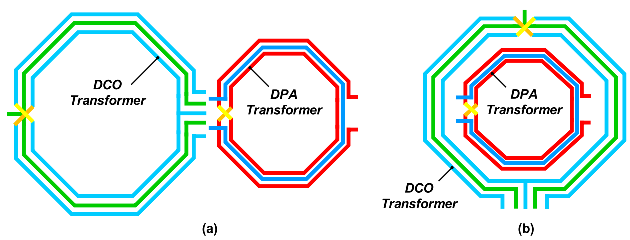

Fig. 1. Layout topology. (a) Conventional side-by-side arrangement of oscillator and PA inductors/transformers. (b) Proposed concentric octagon topology.

The following innovations are introduced: First, to increase power efficiency and reduce area while monolithically integrating all matching-network (MN) components, the DPA adopts a single-ended class-EF topology with a digitally controlled switch resistance. The unavoidable increase in its second harmonic (i.e., HD$_2$) will get self-suppressed by a cross-coupling capacitor C_C across the DPA transformer windings. Second, a concentric octagon topology, as shown in Fig. 1(b), merges the DCO and DPA transformers and places all active components vertically underneath, thus saving ∼50% of die area compared to conventional TXs [4]–[6], in which the inductors/transformers dominate the area [see Fig. 1(a)]. This is far more effective in terms of cost reduction than, for example, with purely vertical integration of associated components underneath their respective transformers [7]. The resultant pulling of DCO by DPA, which can create distortion during non-constant envelope modulation, will be canceled

Manuscript received November 1, 2018; revised February 20, 2019; accepted March 12, 2019. Date of publication April 23, 2019; date of current version June 26, 2019. This work was supported in part by Science Foundation Ireland under Grant 14/RP/I2921. This paper was approved by Associate Editor Alyosha Molnar. *(Corresponding author: Kai Xu.)*

K. Xu and R. B. Staszewski are with the School of Electrical and Electronic Engineering, University College Dublin, Dublin 4, Ireland (e-mail: kai.xu@ucd.ie).

F.-W. Kuo, H.-N. R. Chen, L.-C. Cho, C.-P. Jou, and M. Chen are with Taiwan Semiconductor Manufacturing Company (TSMC), Hsinchu 300, Taiwan (e-mail: fwkuo@tsmc.com).

Color versions of one or more of the figures in this paper are available online at http://ieeexplore.ieee.org.

Digital Object Identifier 10.1109/JSSC.2019.2906803

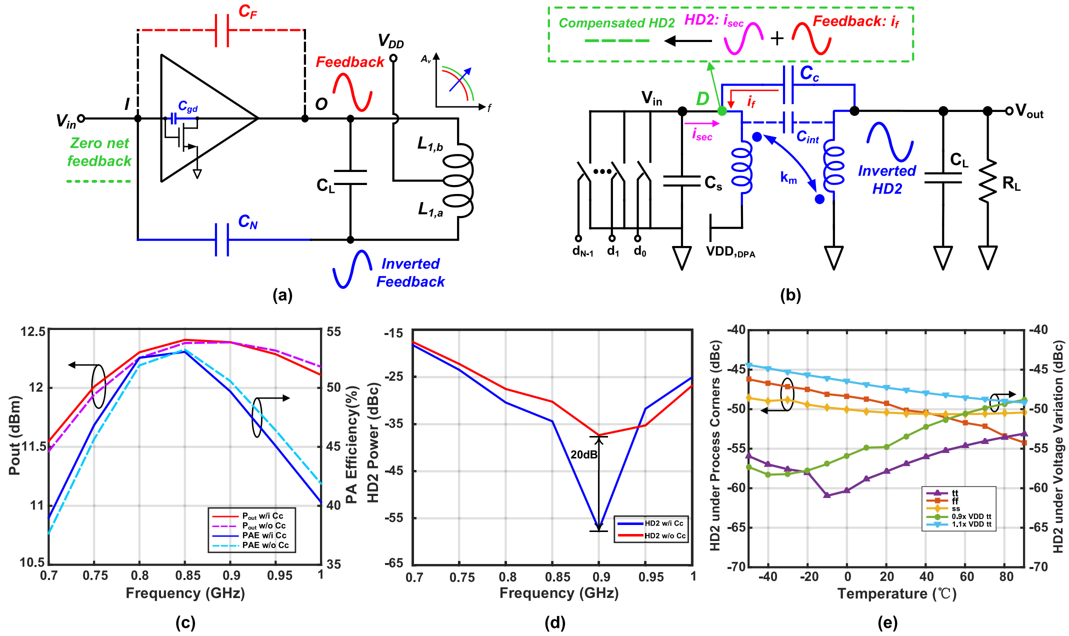

Fig. 2. (a) Conventional RF neutralization. (b) Proposed cancellation technique of HD_2 in single-ended DPA through a cross-coupling capacitor (C_C). (c) and (d) Harmonic balance simulation results. (e) HD_2 suppression under process, voltage and temperature variation.

through a compensating controllable DCO-PA coupling. Third, the DCO uses ULP techniques to bring its power dissipation to below 0.2 mW at 0.3-V supply.

The rest of this paper is as follows. Section II introduces a new second-harmonic suppression technique for the single-ended PA topology. The key innovation of DCO pulling mitigation by steering a PA-to-DCO injection and the low-power characteristic of DCO are investigated in Section III. Section IV reveals the top-level implementation of the prototype with experimental results. Section V wraps up this paper with conclusions.

II. Self-Suppression of HD_2 in Power Amplifier

A differential PA topology is commonly used to suppress second-harmonic (HD_2) emissions that could violate the spurious emission limits of a wireless standard. However, its effectiveness is restricted by the devices' mismatch and asymmetry. A rise-edge-synchronized harmonic calibration (RESHC) technique in [4] compensates the duty-cycle imbalance and phase offset between the PA's differential inputs. To suppress HD_2 in a single-ended topology, one cannot merely rely on filtering by an inductor in a matching network (MN) or even an *LC* bandpass filter. This is due to the limited loaded *Q*-factor of monolithic inductors. Consequently, a conduction-angle (or, equivalently, duty cycle) calibration technique was proposed in [8], although it was demonstrated with off-chip MN components. A further implementation in [9], which combines the duty-cycle calibration and *LC* filtering, managed to cancel out HD_2. However, the output RF power is restricted by the necessarily lower duty cycle. All the above-mentioned techniques are at the expense of an additional system complexity and power consumption.

A. Analogy With Neutralization

An example of a general neutralization technique in high-frequency tuned amplifiers is depicted in Fig. 2(a). A neutralization capacitor C_N is inserted between the (inverted) output and input ports of an amplifier to cancel the undesired coupling in the feedback path caused by a parasitic capacitance C_F, which could be due to a gate–drain capacitance (C_{gd}) in a common-source amplifier. We adapt this technique to achieve our objective of deep HD_2 suppression in a single-ended RF PA, as proposed in Fig. 2(b). A single feedback coupling cancellation (FBCC) capacitor C_C connects across the windings of the PA's MN transformer in the inverting configuration. Unlike in the conventional neutralization technique which copies the inverted output signal into the amplifier's input, thus being effective only near the operating frequency f_0 of the amplifying device [10], the introduced C_C copies the signal from the secondary to the primary winding of the transformer for the purpose of canceling out the the second-harmonic $2f_0$.

The canceling capacitor C_C appears to artificially affect the transformer's inter-winding capacitance C_{int}, where the feedback signal at $2f_0$ has an equal amplitude to the HD_2 component at the common drains of the DPA but is 180° out of phase. In both cases, a perfect cancellation will require precise anti-phase duplicates of the undesired signals. This is in contrast with [11], where the transmission zero inherent with the non-inverting transformer is shifted to reject HD_2. In Fig. 2(a), to achieve zero net feedback at the input, the neutralization capacitor C_N has to be

$$C_N = C_F \frac{L_{1,b}}{L_{1,a}} \tag{1}$$

where the unwanted feedback hinges on the amount of lumped parasitic C_F. For the case of the proposed FBCC, the optimum

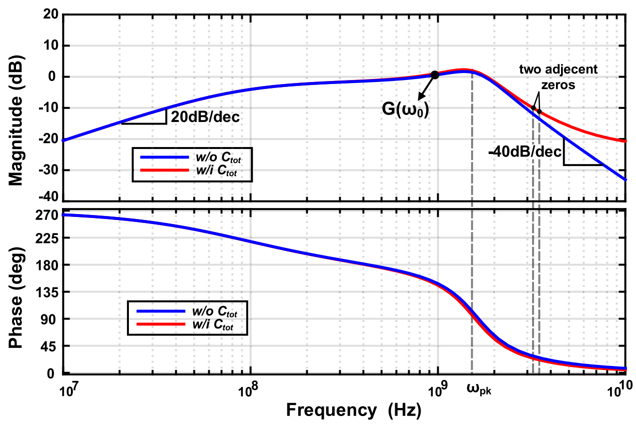

Fig. 3. Bode plot of transfer function $G(s)$ with/without the impact of C_c.

C_C to realize the complete HD_2 suppression will be dependent on the exact strength of the undesired second-harmonic component at the common drain of the switch array incurred by the hard switching and load network. The feedback current is given by

$$\begin{aligned} i_f &= s(C_c + C_{\text{int}}) \cdot (V_{\text{out}} - V_{\text{in}}) \\ &= s(C_c + C_{\text{int}}) \cdot V_{\text{in}} \cdot [G(s) - 1] \end{aligned} \quad (2)$$

wherein $G(s) = V_{\text{out}}/V_{\text{in}}$ indicates the tank's voltage gain transfer function. When considering the effect of FBCC capacitor C_C and interwinding capacitance C_{int}, $G(s)$ is derived in a long formula in (3), as shown at the bottom of this page, with $C_{\text{tot}} = C_C + C_{\text{int}}$, representing the total (inverting) feedback coupling capacitance. By assigning $C_{\text{tot}} = 0$ to both the numerator and denominator of $G(s)$, the transfer function for a case of neglecting the feedback coupling effect can be easily deduced. By simply sweeping C_C in a harmonic balance simulator, we can get the optimum $C_C \approx 247$ fF in this implementation to achieve the HD_2 emission suppressed to < -55 dBc, that is, the feedback current i_f almost perfectly cancels out the HD_2 current i_{sec} at the common drain node. The HD_2 suppression under process, voltage and temperature variations is shown in Fig. 2(e), which proves that it is fairly well contained. At room temperature, the worst case happens at $+10\%$ $V_{DD_{DPA}}$ variation with the HD_2 level of -47 dBc.

B. Transfer Function of the Tank With C_c

After substituting the design parameters of the proposed passive network into $G(s)$, the Bode plot shown in Fig. 3 is obtained. At low frequencies, the magnetizing inductor $L_m = k_m^2 L_p$ of the primary will shunt the energy to ground. Therefore, the first pole can be estimated as $\omega_{p1} = r_p/L_p$ only by taking into account L_p and its equivalent series resistance r_p [12]. By applying $r_p = L_p\omega/Q_p$, $r_s = L_s\omega/Q_s$, $C_{\text{tot}} \ll C_L$ and assuming $Q_p \cdot Q_s \gg 1$, $G(s)$ in (3) can be simplified as a second-order system for frequencies beyond ω_{p1}

$$G(s) \approx \frac{L_s C_{\text{tot}}(1-k_m^2)s^2 + L_s C_{\text{tot}}\omega\left(\frac{1}{Q_p}+\frac{1}{Q_s}\right)s + \frac{M}{L_p}}{L_s C_L(1-k_m^2)s^2 + L_s\left[C_L\omega\left(\frac{1}{Q_p}+\frac{1}{Q_s}\right)+\frac{1-k_m^2}{R_L}\right]s+1}. \quad (4)$$

The complex-conjugate pole pair in (4) with corner frequency

$$\omega_n = \frac{1}{\sqrt{L_s C_L(1-k_m^2)}} \quad (5)$$

introduces a gain peak at frequency ω_{pk}. The damping factor ζ can be easily derived from the denominator polynomial as

$$\zeta = \frac{1}{2}\left[\sqrt{\frac{L_s C_L}{1-k_m^2}}\,\omega\left(\frac{1}{Q_p}+\frac{1}{Q_s}\right)+\frac{1}{R_L}\sqrt{\frac{L_s}{C_L}(1-k_m^2)}\right]. \quad (6)$$

The peak location ω_{pk} is related to the corner frequency ω_n as

$$\omega_{\text{pk}} = \omega_n\sqrt{1-2\zeta^2}. \quad (7)$$

With $\zeta \approx 0.4$ in this design, the peak is located roughly at $\omega_{\text{pk}} \approx \omega_n$. The Bode plot also indicates that C_C (or C_{tot}) has no substantial effect on the frequency response below ω_{pk}, which lies higher than the fundamental resonance frequency $\omega_0 = 2\pi f_0$ designated for frequency selection of the signal. Consequently, the addition of optimal C_C will cancel out the undesired second harmonic (i.e., $2f_0$) with only negligible performance degradation of the desired signal at f_0. This observation is supported by circuit simulation results shown in Fig. 2(c), which reveal only 1% efficiency drop by adding C_C.

The numerator of (3) also turns out to be a second-order polynomial after taking C_{tot} into account but with a totally different behavior compared to that of the denominator. Zeros of the system are the roots of $N(s) = 0$ with $N(s)$ indicating the numerator polynomial. To simplify the analysis, we rewrite the equation to a more general case $as^2 + bs + c = 0$, where the coefficients $a, b,$ and c can be easily mapped to the coefficients of $N(s)$. Accordingly, solutions of $N(s)$ are given by $s = (-b \pm \sqrt{b^2-4ac})/2a$. For a transformer in the inverting configuration, the mutual inductance between the primary and secondary windings is negative (i.e., $M < 0$), as a result, $c = M/L_p < 0$. Given that $a = L_s C_{\text{tot}}(1-k_m^2) > 0$ and $b = L_s C_{\text{tot}}\omega(1/Q_p + 1/Q_s) > 0$, it is easy to predicate that there are two real zeros of $G(s)$, thereinto $z_1 < 0$ signifies the zero located in the left half-plane (LHP) of the s-domain and the other zero $z_2 > 0$ lies in its right half-plane (RHP).

$$G(s) = \frac{[(L_pL_s - M^2)s^2 + (L_pr_s + L_sr_p)s + r_pr_s]C_{\text{tot}}s + Ms}{(L_pL_s - M^2)(C_{\text{tot}}+C_L)s^3 + \left[(L_pr_s+L_sr_p)(C_{\text{tot}}+C_L)+\frac{L_pL_s-M^2}{R_L}\right]s^2 + \left[L_p+(C_{\text{tot}}+C_L)r_pr_s+\frac{L_pr_s+L_sr_p}{R_L}\right]s + r_p + \frac{r_pr_s}{R_L}} \quad (3)$$

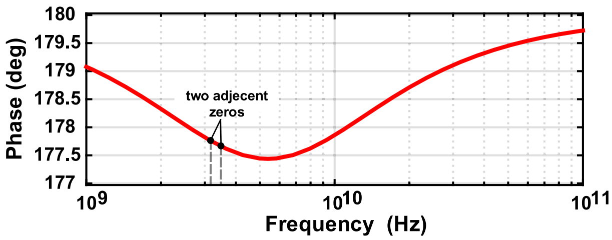

Fig. 4. Bode phase plot for the two adjacent zeros.

Considering the fact that C_{tot} is on the order of 10^{-15} F, this results in $b^2 \ll -4ac \rightarrow |b| \ll \sqrt{-4ac}$. Then, the solutions of $N(s) = 0$ can be estimated as

$$z_{1,2} \approx \pm\sqrt{-\frac{c}{a}} = \pm\sqrt{\frac{-k_m n}{L_s C_{\text{tot}}\left(1-k_m^2\right)}} \tag{8}$$

where n represents the turns ratio of the transformer. This highlights that the two real zeros z_1 and z_2, with $|z_1| > |z_2|$, share rather close distance to the imaginary axis in the s-plane. The magnitude asymptotes of RHP zeros are identical to those of LHP zeros with a +20-dB/dec slope. However, the phase asymptotes of RHP zeros show similar behavior as LHP real poles, which result in a −90° phase shift. Because of the complex-conjugate pole pair previously discussed, the voltage gain will drop with a −40-dB/dec slope shown as the blue line in Fig. 3. Nevertheless, this gain drop will be compensated by the two C_{tot}-originated adjacent zeros with a +20 dB/dec increase in the slope (note that these zeros do not arise if $C_{\text{tot}} = 0$). As indicated by the red curve, when it encounters the two zeros at around 3.5 GHz, instead of quickly rolling off, it becomes flattened. The unexpected negative phase jump due to the RHP zero z_2 will also be canceled out by the nearby LHP zero z_1, as illustrated in Fig. 4. Thus, the total phase response of $G(s)$ will be predominately contributed by the poles of the passive network.

Equation (8) reveals that C_c, being the design-adjustable part of C_{tot}, can certainly increase the feedback at $2f_0$ through shifting the zero locations thus to alter the rolling-down slope of the gain response. Beyond that, C_L can also influence the feedback at $2f_0$ through shifting the peak location of $G(s)$ adjusting the rolling-up slope of the gain response before it rolls down, which is manifested by (5)–(7). As C_c is fixed in this specific implementation, C_L can be tuned to maintain the HD_2 rejection when the carrier frequency of the DPA varies. In addition, $-k_m n > 1$ and $C_{\text{tot}} \ll C_L$ in (8) and (5) suggests that the frequency of the gain peak will be lower than that of the zeros, $\omega_{\text{pk}} < |z_{1,2}|$. To the best of authors' knowledge, this is the first thorough quantitative discussion about the effects of interwinding capacitance in a general transformer with operational loading and nonidealities [13], [14].

C. Quasi-Class-$EF_{2,3}$ Switching PA

In comparison with current-source-based PAs, the class-E derived switching PA has distinguished itself in terms of high power efficiency due to the non-overlap between the switch' voltage and current waveforms. The disadvantage here, however, lies in the peak drain voltage V_D during the off-switch times, which can be as high as 3.56 times the power supply ($V_D \approx 3.56\ V_{\text{DD}}$) [15]. In response, a hybrid of class-E with class-F or class-F^{-1} was reported to reduce the peak voltage to $\sim 2V_{\text{DD}}$ and to benefit from waveform shaping through harmonic tuning [16]. As for the single-ended topology, the hybrid class-E/F PA (see the definitions in [16]) does not show its superiority over class-EF, which cannot exploit the differential-mode and common-mode impedances in a single-load network to perform distinct reactions under odd and even harmonic stimuli. A transformer-based power combining network can incorporate the RF choke L_{RFC} and fundamental frequency tuning L_{tn} inductors of the conventional class-E network into the magnetic inductance L_m at its primary coil. Meanwhile, L_{add} can be absorbed into the leakage inductance L_{leak} and C_{tn} equivalently shifted to the secondary as C_L [17]. Furthermore, the capacitor C_s in parallel with the switch is designed to resonate out at near the third-harmonic frequency $3f_0$, taking advantage of the other resonant tank inherently within T_1.

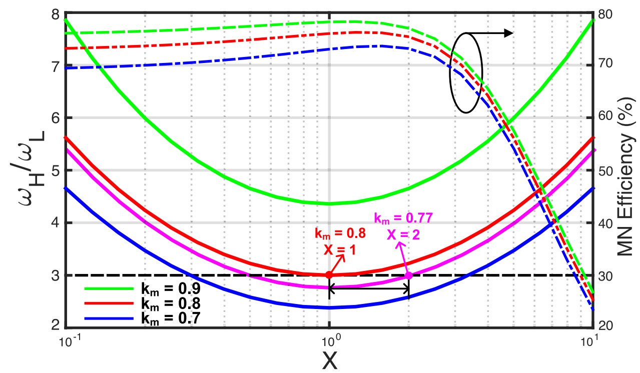

Fig. 5. Ratio of tank resonance frequencies and efficiency versus X-factor for various k_m.

The transformer T_1 should also provide the required load impedance transformation of R_L to the switching devices as $r_L \approx (R_L + r_s) \cdot k_m^2/n^2$ in order to optimally deliver a certain desired amount of RF power. For a targeted $P_{\text{out}} \approx 12$ dBm under $V_{\text{DD}} = 0.85$ V, a step-up transformer with turns-ratio $n > 1$ should be used to lower r_L (note that with no impedance transformation, the maximum delivered power would only be $P_{\text{out,max}} = (V_{\text{DD}} - V_{\text{knee}})^2/2R_L \approx 5.6$ dBm with $V_{\text{knee}} = 0.1$ V.) By assuming a low-loss case ($r_p, r_s, r_{C_L}, r_{C_s} \rightarrow 0$), two possible resonant frequencies in a transformer were described in [12] as

$$\omega_{H/L}^2 \approx \frac{1+\left(\frac{L_s C_L}{L_p C_s}\right) \pm \sqrt{1+\left(\frac{L_s C_L}{L_p C_s}\right)^2+\left(\frac{L_s C_L}{L_p C_s}\right)\left(4k_m^2-2\right)}}{2L_s C_L\left(1-k_m^2\right)} \tag{9}$$

where ω_H and ω_L represent the higher and lower resonance frequencies, respectively. Similarly, we define X-factor as $X = (L_s/L_p) \cdot (C_L/C_s)$, thus the ratio of resonant frequencies ω_H/ω_L can be easily obtained that is purely a function of X-factor and the coupling coefficient k_m. Given that the turns ratio $n = \sqrt{L_s/L_p}$ is initially decided by the targeted P_{out}, X-factor will be eventually a subject to the tuning capacitance ratio C_L/C_s. The influence of X-factor on ω_H/ω_L and the

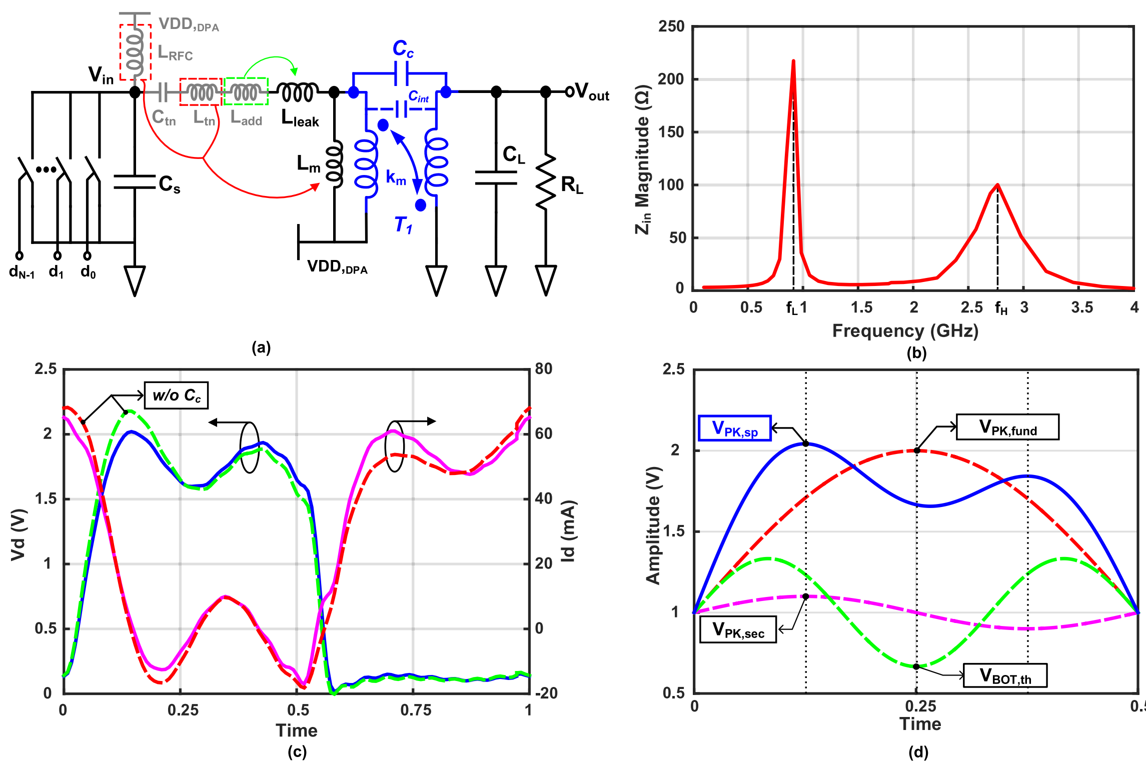

Fig. 6. Transformer-based load transformation network. (a) Incorporation of loading network of class-E into transformer [17]. (b) Magnitude of the input impedance, Z_{in}. (c) Drain voltage and switch current waveforms. (d) Superimposed harmonics of the drain voltage.

matching network efficiency η_M (Q_p and Q_s assumed to be 10) for various k_m are both plotted in Fig. 5. No solutions of X can be found for $\omega_H/\omega_L = 3$ when $k_m > 0.8$ in order to realize a second impedance peak at the third harmonic. On the other hand, the matching network efficiency η_M is positively correlated with k_m and will reach its peak value for $1 \leqslant X \leqslant 2$ shown with the dashed lines. To preserve a relatively high efficiency, it is desirable to design X-factor within the region $1 \leqslant X \leqslant 2$ which corresponds to a coupling factor range $0.8 \geqslant k_m \geqslant 0.77$ in order to achieve the impedance peak at $3f_0$. In reality, the resonant frequencies of the tank $\omega_{H,L}$ will also be influenced by the series resistance (r_p, r_s) of the two windings and the total interwinding capacitance C_{tot}, thus there could be a slight offset from the X-factor depicted in Fig. 5 in order to meet $\omega_H/\omega_L = 3$ under certain k_m. The choice of C_L follows a similar way as in [2], mainly to balance the effects of loaded Q-factor ($Q_L = R_L C_L \omega_0$) on the matching network efficiency η_M and the frequency selection. In this paper, T_1 in Fig. 6(a) is designed as $L_s/L_p = n^2 \approx$ 7.5 nH/5.5 nH with $k_m \approx 0.8$. The capacitance parameters are $C_L \approx 3.5$ pF and $C_s \approx 2.8$ pF. Now, that the total interwinding capacitance $C_{\text{tot}} \approx 0.11C_s$ ($C_{\text{tot}} = C_c + C_{\text{int}} \approx 320$ fF) and $n \approx 1.2$ are both fairly small, it is acceptable to ignore the multiplicative equivalent capacitance subject to the Miller effect at the primary side of T_1. Consequently, we reach $X \approx 1.46$. Fig. 6(b) illustrates the simulated Z_{in} of the transformer-based load network seen by the common drains of the switching PA for the $X \approx 1.46$ value that satisfies the resonance frequency ratio $\omega_H/\omega_L = 2\pi f_H/2\pi f_L = 3$.

TABLE I

WAVEFORM FACTORS FOR VARIOUS HYBRIDS OF CLASS-E AND CLASS-F AMPLIFIERS

	F_V	F_I	F_C
E	3.56	1.54	3.14
E/F_2	3.67	1.48	1.13
E/F_3	3.14	1.52	3.14
E/$F_{2,3}$	3.13	1.47	2.31
E/$F_{2,4}$	3.43	1.46	0.97
E/$F_{2,3,4}$	3.08	1.45	1.18
Quasi-EF$_{2,3}$	**2.38**	**1.46**	**1.68**

Moreover, the proposed C_C manages to suppress the second harmonic both at the common drain and output, which effectively shunts the energy of second harmonic to ground. Following the nomenclature for class-EF in [16], where the load seen by the common drain of the switches is an open circuit at odd harmonics and a short circuit at even harmonics, we name the proposed switching PA as a quasi-class-EF$_{2,3}$ PA. As there is no real short circuit at the second harmonic, we term it "quasi." To evaluate the performance of the quasi-class-EF$_{2,3}$ PA, a comparison of waveform factors $F_V \equiv V_{\text{pk}}/V_{\text{DC}}$, $F_I \equiv I_{\text{rms}}/I_{\text{DC}}$ and $F_C = P_{\text{out}}/V_{\text{DC}}^2/Z_C$ [16] is made among various tuning strategies in Table I. Smaller numbers indicate better performance. The simulated drain voltage and switch current waveforms are shown in Fig. 6(c). The time on the x-axis is normalized to the switching period,

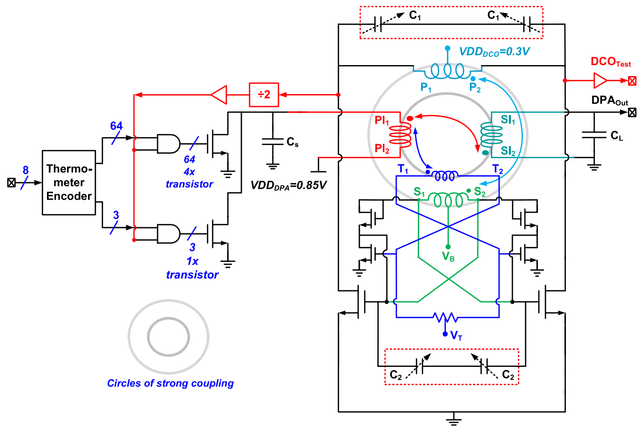

Fig. 7. Schematic of the merged DPA-DCO with the proposed mitigation of injection pulling through the magnetic coupling feedback.

T_{sw}. V_d is the superposition of V_{DC}, fundamental frequency voltage v_{fund}, and other higher order harmonic components. When only considering the first three harmonics and ignoring higher orders, which are relatively small, V_d is approximately decomposed into three sinusoidal waves with frequencies at the first three harmonics shown in Fig. 6(d). It appears that the voltage peak of fundamental $V_{\text{pk,fund}}$ is reduced at the presence of third harmonic. Interestingly, the superimposed voltage $v_{\text{sp}} = V_{\text{DC}} + v_{\text{fund}} + v_{\text{sec}} + v_{\text{thd}}$ has its peak $V_{\text{pk,sp}}$ situated around the second-harmonic peak $V_{\text{pk,sec}}$, which is at $1/4 \cdot T_{sw}$, thus indicating that HD_2 will also play an important role in $V_{\text{pk,sp}}$. The rejection of HD_2 by means of adding the proposed C_C could benefit F_V reduction up to 24%.

III. Pulling Mitigation of DCO by DPA

The ULP operation is paramount for IoT oscillators. The power drain of an RF oscillator is [2]: $P_{DC} = 2V_{\text{DD}}/R_p \cdot \alpha_v/\alpha_i$, so it calls for: low supply voltage V_{DD}, high parallel resistance R_p of the tank, low-voltage efficiency α_v, and high-current efficiency α_i. However, $\alpha_v\alpha_i$ should be maximized to avoid penalty on FoM in that α_v should not be too low. A 0.3-V V_{DD} is achieved by adopting a transformer feedback topology. Moreover, $R_p = L_p\omega_0\, Q_t$ can be magnified through increasing the tank inductance and Q-factor. Multiple turns and large diameter are preferable for large inductors with high Q-factor, thus a transformer with 2:3 turns-ratio and 450 μm inner radius is deployed in the 1.8-GHz DCO, as shown in Fig. 7. The tank's $R_p \approx 1.5$ kΩ is reached with the primary winding inductance L_p of 10 nH and Q of 12. The tradeoff between P_{DC} and die area due to the enlarged inductor is relieved by the proposed concentric octagon layout topology and by placing all other active devices vertically below the region of DCO's inner diameter.

Compared to the conventional side-by-side (i.e., lateral) arrangement of the oscillator and PA, a stronger magnetic coupling that causes the DCO pulling by the DPA at near $2f_0$ can be expected in this compact topology. To keep the coupling factor $k_{m,4}$ reasonably low ($k_{m,4} \approx 0.16$ as per EMX simulations), a distance of 150 μm is reserved in between the outermost turn ($PI_1 - PI_2$) of the DPA transformer and the innermost turn ($S_1 - S_2$) of the DCO transformer depicted in Fig. 8. To help it further, an extra small coil ($T_1 - T_2$) is inserted between the two transformers to sense the coupling, and to send an amplified but inverted signal back to the DCO transformer. The compensating strength is controlled by a V_T bias such that the magnetic coupling at the second harmonic between the DPA and DCO transformer windings can be canceled by the second-harmonic injection into the DCO.

Notwithstanding the amount of HD_2 already suppressed to a relatively small value through the proposed C_C capacitor both at the common drain node and output nodes of the DPA, i.e., PI_1 and SI_1 in Fig. 8, the remaining injection pulling still could be significant since even a weak injection strength can catastrophically impact the TXs performance [18]. Note that the dominant coupling path lies in the magnetic coupling from ($PI_1 - PI_2$) to ($S_1 - S_2$) rather than that from ($SI_1 - SI_2$) attributed to 5 dB higher HD_2 power at the drain node as per simulations.

The scenario of a free-running LC oscillator under injection pulling is shown in Fig. 9(a). The phasor V_{tot} is the composite vector of the oscillator phasor, V_{osc}, and AM-modulated aggressor phasor, V_{inj}. In the absence of aggressor, V_{tot} aligns with V_{osc}, i.e., ϕ is zero. Once the oscillator encounters the second harmonic of the PA, either through a parasitic or magnetic coupling, there will be an additional phase shift (a non-zero ϕ) between V_{osc} and V_{tot} which violates the Barkhausen criterion at ω_0. This will shift the oscillation frequency lower to ω_{inj}. Upon reaching the steady state, the oscillation frequency $\omega_{\text{out}} = \omega_{\text{inj}}$ indicating that V_{osc}, V_{inj}, and V_{tot} rotate at the same rate with a constant angular displacement θ between V_{osc} and V_{inj}. However, the phase shift ϕ will not be constant under the time-varying AM–FM conversion. A stronger injection V'_{inj} will introduce a different phase shift ϕ'. In [19], the DCO is exposed to a parasitic frequency modulation (FM) resulting from injection pulling of an amplitude modulated (AM) aggressor, mainly the second harmonic at the DPA output. The solution was to delay the DPA clock to align it with the DCO phase for the lowest aggressor-victim sensitivity.

To gain insight into the aforementioned mechanism, a general mathematical model of injection-pulled free-running oscillator described in [18]– [20] is retrospected

$$\omega_{\text{out}} = \omega_0 - \frac{\omega_0}{2 \cdot Q} \cdot \frac{V_{\text{inj}}}{V_{\text{osc}}} \cdot \sin\theta \tag{10}$$

$$\omega_{\text{out}} = \omega_0 + \omega_{\text{pulling}} \tag{11}$$

where Q is the quality factor of the LC tank at undisturbed frequency ω_0, which may vary under an FM modulation, V_{osc} and V_{inj} are the fundamental amplitude of the oscillator signal and the envelope of the injection, respectively, with θ as the instantaneous angle between them. Note that V_{inj} is also time-varying if the TX undergoes AM modulation. The expression ω_{pulling} in (11) is equivalent to the second term in (10) representing the parasitic FM due to the AM–FM conversion. Previous approaches dedicated to reduce the AM-induced FM pulling can be mapped onto (10). For example, a digitally controlled delay (DCD) stage was inserted between the DCO and DPA in [19] to adjust the phase of ω_{inj} such that its

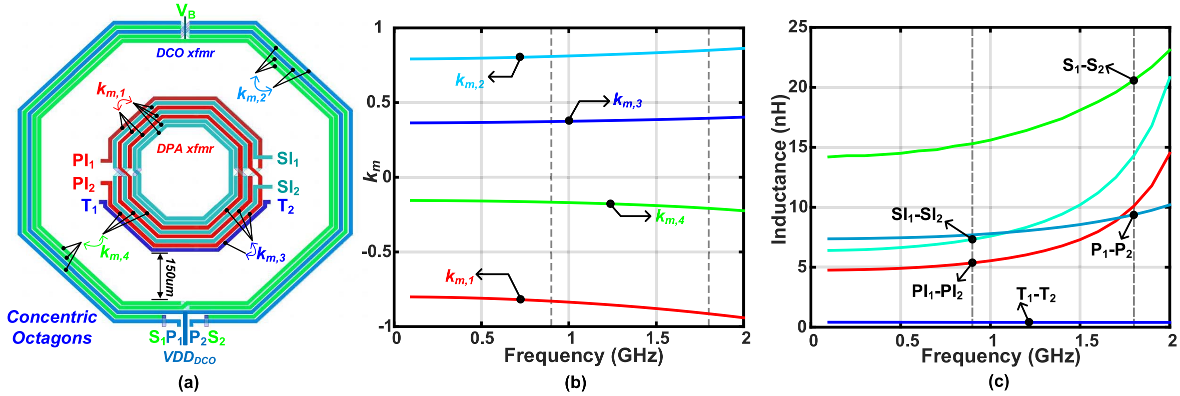

Fig. 8. Inductances and coupling factors of the concentrically laid out transformers. (a) Concentric octagon topology. (b) Coupling factors. (c) Inductances.

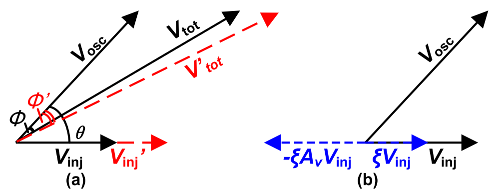

Fig. 9. *LC* oscillator under injection pulling. (a) AM–FM conversion mechanism [19]. (b) Concept of pulling mitigation through magnetic coupling compensation.

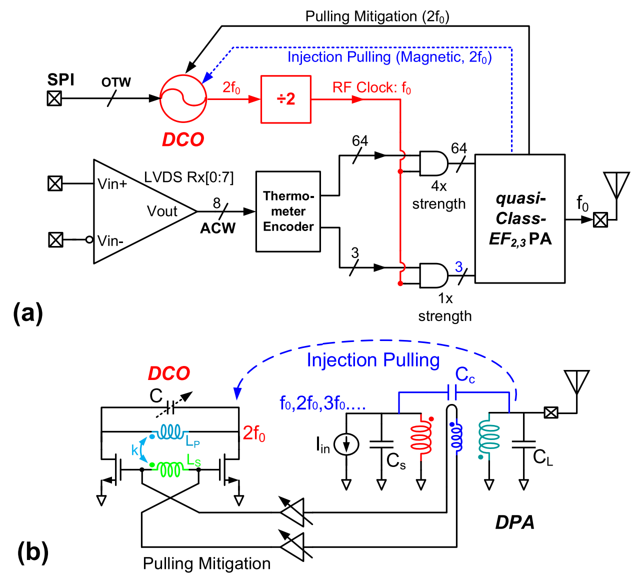

Fig. 10. (a) Top-level diagram of the proposed DCO-DPA. (b) Simplified pulling mitigation concept between the DPA and DCO.

phase angle (θ) related to ω_{out} equals zero or π, which means the second term in (10) is close to zero.

The method proposed in this paper is distinct from the previous solutions and indicated in Fig. 9(b). By virtue of the extra small coil ($T_1 - T_2$ in Fig. 7) between the two transformers, an accurate duplicate of the injection aggressor V_{inj} can be acquired across the terminals of the coil but with a scaling factor ξ. Assuming the aggressor finds its way to the DCO through a coupling path represented by transfer function $H(s)$, then ξ can be expressed as

$$\xi = \frac{1}{H(s)} \cdot \frac{n_{\mathrm{PI,T}}}{k_{m,3}} \tag{12}$$

where $n_{\mathrm{PI,T}}/k_{m,3}$ is exactly the nonideal turns ratio between the ($T_1 - T_2$) coil and the outermost turn of the DPA transformer ($\mathrm{PI}_1 - \mathrm{PI}_2$) with $n_{\mathrm{PI,T}} = L_T/L_{\mathrm{PI}} = 0.4$ nH/10 nH and $k_{m,3} = 0.4$ at $2f_0$. Under a scenario dominated by magnetic coupling, $H(s) \approx n_{\mathrm{PI,S}}/k_{m,4}$. The duplicate signal $\xi \cdot V_{\mathrm{inj}}$ is then amplified by $-A_V$ and sent back to the oscillator where it will cancel the aggressor V_{inj}. For simplicity, we rewrite (10) as: $\omega_{\mathrm{out}} = \omega_0 + \mu \cdot V_{\mathrm{inj}}$. After taking into account the parasitic injection, we have

$$\omega_{\mathrm{out}} = \omega_0 + \mu \cdot V_{\mathrm{inj}} + \mu \cdot (-\xi \cdot A_V) \cdot V_{\mathrm{inj}}. \tag{13}$$

The AM–phase modulation (PM) injection pulling can be minimized when $\xi \cdot A_V = 1$. The amplification is realized with a simple common-source stage with a diode-connected load, while the gain $-A_V$ is controllable through tuning the V_T bias. Once V_T is optimized for certain V_{inj}, it will hold for any complicated AM modulation scheme as $V_{\mathrm{T,opt}}$ has no dependence on the injection strength.

IV. Experimental Results

A. Proposed DCO-DPA for Sub-Gigahertz IoT TX

A block diagram of the proposed merged DCO-DPA is depicted in Fig. 10(a). The DCO provides the RF carrier clock and the DPA realizes the digital modulation of the carrier's envelope. Instead of oscillating at the PA's carrier frequency f_0 (i.e., ~0.9 GHz), the DCO tank's Q-factor is optimized at $2f_0$ followed a ÷2 divider for the purpose of smaller area and lower phase noise (PN) under same power budget [1]. A simple 8-bit single-ended quasi-class-$EF_{2,3}$ DPA is adopted to maximize the efficiency. The concentric octagon layout topology is realized by placing the DPA MN transformer within the inner diameter of the DCO transformer. The HD_2 emission at $2f_0$ due to the nonlinearity of DPA switches can potentially injection-pull the DCO through magnetic coupling. The 256 amplitude steps of the DPA are achieved by two unit-weighted segments of 64 4× and three 1× transistors [21]. In this way, the total number of the transistors in the PA array can be reduced from 256 to 64 + 3 = 67,

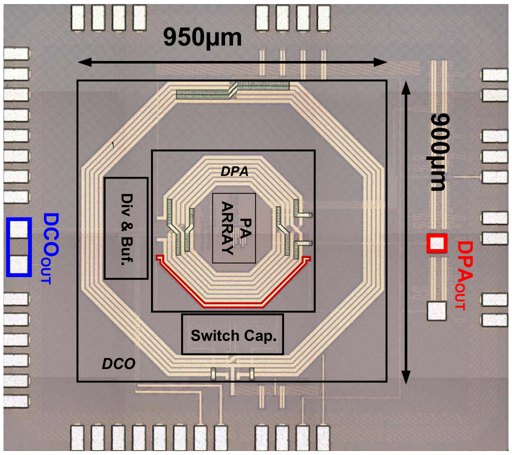

Fig. 11. Chip micrograph of the sub-gigahertz DCO-DPA.

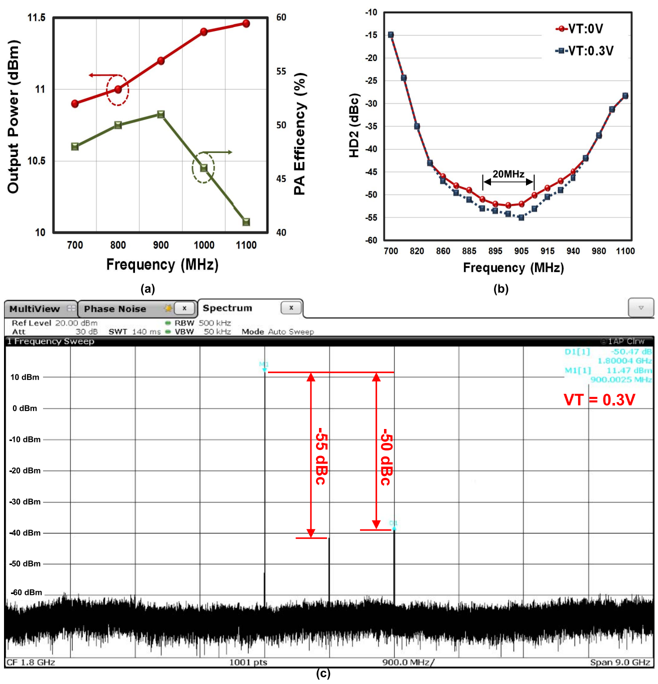

Fig. 12. DPA output-port measurements. (a) DPA output power and efficiency. (b) and (c) HD_2 emission performance at V_T= 0 V and V_T= 0.3 V (i.e., compensating path turned off/on).

which helps to alleviate the overall routing complexity. All other blocks shown in Fig. 10(a) are also integrated on-chip.

B. Measurement Results

The chip is fabricated in 16-nm FinFET CMOS, occupying 0.85 mm^2 in total, as shown in the die photo in Fig. 11. The single-ended sub-gigahertz DPA achieves 51% total power efficiency at 11.5-dBm RF output and 0.85-V supply. The measured HD_2 emissions, shown in Fig. 12(b), are < -52 dBc ($V_T = 0$ V, thus disabling the controllable DPA-to-DCO injection of the second harmonic), which verifies the effectiveness of the FBCC capacitor. A < -50-dBc HD_2 emission level is maintained over ±10-MHz offset from the carrier, indicating that this technique can be applied to wideband modulation. The coupling compensation path can further help to suppress the HD_2 to < -55 dBc ($V_T = 0.3$ V).

TABLE II

COMPARISON WITH STATE-OF-THE-ART SUB-GIGAHERTZ TXS

	This work	ISSCC'16 [1]	ISSCC '16 [5]	VLSI'17 [4]	RFIC'17 [6]	Units
CMOS Technology	16nm FinFET	40nm	180nm	40nm	65nm	
Supply	0.85/0.3	1	2.2-3.6	3-3.6	1.2	V
RF Band	sub-GHz	sub-GHz	sub-GHz	sub-GHz	sub-GHz	
PA Architecture	Single-ended Quasi-Class $EF_{2,3}$	Differential SC-DPA	Single-ended Class F	Differential RESHC-Class E	Differential Class D	
Peak RF Power	11.5	8	17	20	17.1	dBm
Peak PA Efficiency	51	45	42.3	43 [a]	51.7 [b]	%
HD2	-55	N/A	N/A	-59.2	N/A	dBc
Modulation	64QAM OFDM	64QAM OFDM	FSK	FSK	π/4-DQPSK	
Bandwidth	2MHz	2MHz	8.5kHz	12kHz	1MHz	
Average P_{out}	5	0	N/A	N/A	6.3	dBm
EVM	3.7%	4.4%	FSK Error 0.8%	FSK Error 1.5%	6.98%	
TX Size	0.85	0.72 [c]	2 [c]	1.3 [c]	3 [d]	mm^2
On-chip Matching	Yes	No	No	No	Yes	

a: TX efficiency; b: drain efficiency only; c: external matching needed; d: graphically estimated.

The measured PN of the 1.8-GHz DCO is plotted in Fig. 13(a). At a 0.3-V supply, it reaches −116 dBc/Hz at 1-MHz offset from 1.8-GHz carrier while consuming 195 uW. The DCO covers a frequency tuning range from 1.1 to 2.1 GHz. The AM-induced injection pulling spurs are measured at the DCO output port when the DPA toggles all the switches at a $f_m = 5$ MHz rate. The measured $f_c \pm f_m$ spurs are reduced from −35 dBc at $V_T = 0$ V (no compensation) to −57 dBc at $V_T = 0.3$ V, which validates the proposed pulling mitigation method [Fig. 13(b)]. Different injection strengths are inspected by controlling the power of the AM signal through the amplitude control word controls of the DPA (only tuning the MSB codes here), it indicates that there is one universal optimum $V_T = 0.3$ V for various levels of AM signal power from −10 to 11 dBm in order to suppress the AM-induced spurs. All these spurs are below −50 dBc, as shown in Fig. 13(c). The extra power consumption of the DCO due to engaging of the pulling mitigation path is only 5 μW.

The measured modulation spectrum of a transmitted 2-MHz 64-QAM orthogonal frequency division multiplexing (OFDM) signal is shown in Fig. 14. By engaging the pulling compensation path, the measured error vector magnitude (EVM) improves 3.5% at 0-dBm output power, which is a 12.5% improvement compared with the 4% EVM when $V_T = 0$ V. With the help of pulling mitigation, EVM < 4% is maintained for output power levels of up to 5-dBm, as depicted in Fig. 15. In case of a more visible pulling effect when a 100-kHz 64-QAM signal at 5-dBm is measured, the EVM improves from 3.35% to 1.5% at 5-dBm RF output power through turning on the compensating path. The DCO-DPA performance is summarized in Table II and favorably compares to state-of-the-art sub-gigahertz TXs. The presented concentrically laid out DCO-DPA solution offers 3× area reduction compared to recent publication [6] with on-chip matching. The deep HD_2 (< −55 dBc) rejection is achieved without resorting to complex circuitry or calibration and with an insignificant increase in power consumption. Together with the magnetic coupling compensation of injection pulling, our design shows

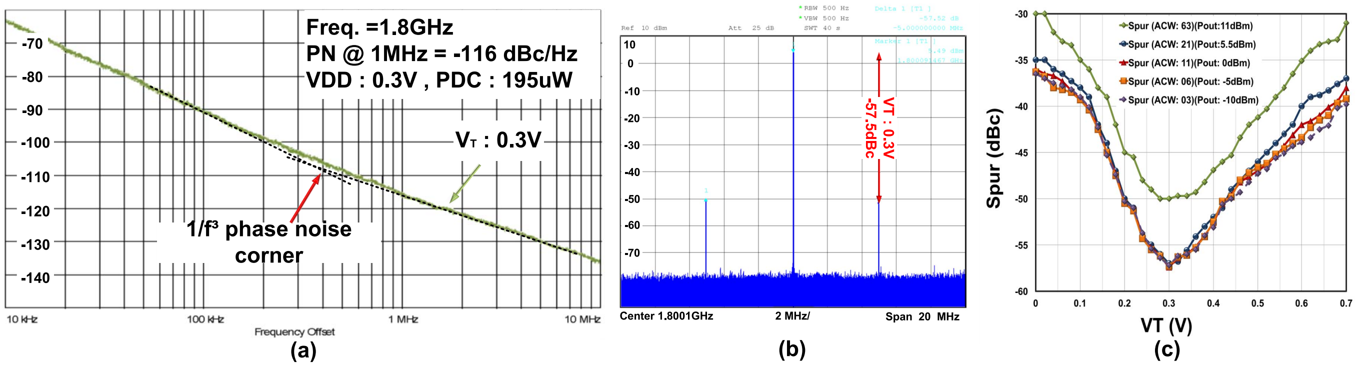

Fig. 13. DCO output-port measurements. (a) DCO PN. (b) and (c) DPA-induced (by 5-MHz AM) pulling mitigation performance with tunable V_T.

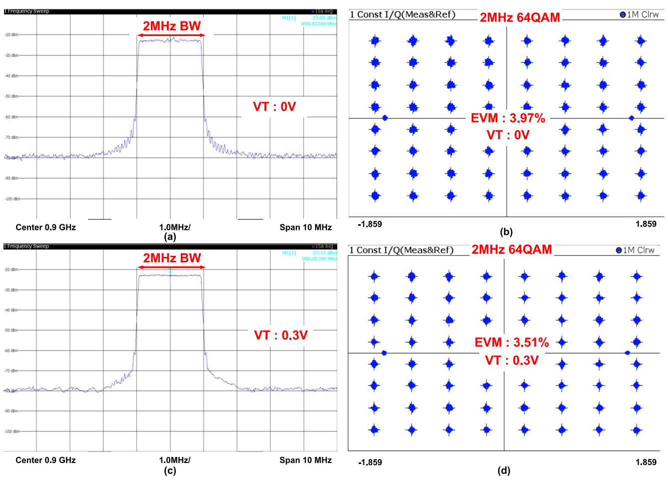

Fig. 14. (a) and (c) Output spectra and (b) and (d) constellation diagrams under 2-MHz 64-QAM modulation at V_T= 0 V and V_T= 0.3 V (i.e., compensating path turned off/on, respectively).

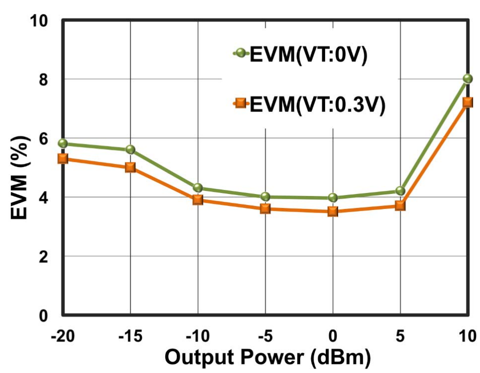

Fig. 15. EVM versus output power with the compensating path turned off/on.

better EVM at 3× higher average RF power with OFDM modulation [1].

V. Conclusion

A compact merged DCO-DPA circuitry with a fully integrated matching network for a sub-gigahertz IoT TX is introduced in this paper. It achieves the highest PA efficiency, thanks to its single-ended configuration while maintaining sufficiently high HD_2 suppression by means of the proposed FBCC capacitor. The lowest DCO power consumption and the smallest system area are achieved via the proposed concentric layout topology. The resulting coupling can be virtually eliminated by the proposed controllable DPA-to-DCO injection.

Acknowledgment

The authors would like to thank Integrand Software for the EMX license.

References

[1] A. Ba *et al.*, "A 1.3nJ/b IEEE 802.11ah fully digital polar transmitter for IoE applications," in *IEEE Int. Solid-State Circuits Conf. (ISSCC) Dig. Tech. Papers*, 2016, pp. 440–441.

[2] M. Babaie *et al.*, "A fully integrated Bluetooth low-energy transmitter in 28 nm CMOS with 36% system efficiency at 3 dBm," *IEEE J. Solid-State Circuits.*, vol. 51, no. 7, pp. 1547–1565, Jul. 2016.

[3] J. Yin, S. Yang, H. Yi, W.-H. Yu, P.-I. Mak, and R. P. Martins, "A 0.2 V energy-harvesting BLE transmitter with a micropower manager achieving 25% system efficiency at 0 dBm output and 5.2 nW sleep power in 28 nm CMOS," in *IEEE Int. Solid-State Circuits Conf. (ISSCC) Dig. Tech. Papers*, Feb. 2018, pp. 450–452.

[4] M. Mizokami, T. Uozumi, Y. Yamashita, K. Shibata, and H. Sato, "A 43%-efficiency 20 dBm sub-GHz transmitter employing rise-edge-synchronized harmonic calibration with 33.3% duty cycle," in *Symp. VLSI Circ. Dig.*, Jun. 2017, pp. C304–C305.

[5] N. Kearney *et al.*, "A 160-to-960MHz ETSI class-1-compliant IoE transceiver with 100 dB blocker rejection, 70 dB ACR and 800 pA standby current," in *IEEE Int. Solid-State Circuits Conf. (ISSCC) Dig. Tech. Papers* , Jan./Feb. 2016, pp. 442–443.

[6] M. Wei *et al.*, "A fully integrated reconfigurable low-power Sub-GHz transceiver for 802.11ah in 65 nm CMOS," in *Proc. IEEE Radio Freq. Integr. Circuits Symp.*, Jun. 2017, pp. 240–243.

[7] F. W. Kuo *et al.*, "A bluetooth low-energy transceiver with 3.7-mW all-digital transmitter, 2.75-mW high-if discrete-time receiver, and TX/RX switchable on-chip matching network," *IEEE J. Solid-State Circuits.*, vol. 52, no. 4, pp. 1144–1162, Apr. 2017.

[8] A. Ba, V. K. Chillara, Y. Liu, H. Kato, K. Philips, and R. B. Staszewski, "A 2.4 GHz class-D power amplifier with conduction angle calibration for -50 dBc harmonic emissions," in *Proc. IEEE Radio Freq. Integr. Circuits Symp.*, Jun. 2014, pp. 239–242.

[9] M. Silva-Pereira and J. Caldinhas Vaz, "A single-ended modified class-E PA with HD2 rejection for low-power RF applications," *IEEE Solid-State Circuits Lett.*, vol. 1, no. 1, pp. 22–25, Jan. 2018.

[10] T. H. Lee, *The Design of CMOS Radio-Frequency Integrated Circuits*. Cambridge, U.K.: Cambridge Univ. Press, 1998.

[11] K. Xu, J. Yin, P.-I. Mak, R. B. Staszewski, and R. P. Martins, "A 2.4-GHz single-pin antenna interface RF front-end with a function-reuse single-MOS VCO-PA and a push-pull LNA," in *Proc. IEEE Asian Solid-State Circuits Conf. (A-SSCC)*, Nov. 2018, pp. 293–294.

[12] M. Babaie and R. B. Staszewski, "A class-F CMOS oscillator," *IEEE J. Solid-State Circuits.*, vol. 48, no. 12, pp. 3120–3133, Dec. 2013.

[13] J. R. Long, "Monolithic transformers for silicon RF IC design," *IEEE J. Solid-State Circuits.*, vol. 35, no. 9, pp. 1368–1382, Sep. 2000.

[14] X. Xiao *et al.*, "A 65-nm CMOS wideband TDD front-end with integrated T/R switching via PA re-use," *IEEE J. Solid-State Circuits.*, vol. 52, no. 7, pp. 1768–1782, Jul. 2017.

[15] N. O. Sokal, "Class E high-efficiency power amplifiers, from HF to microwave," in *IEEE MTT-S Int. Microw. Symp. Dig.*, Jun. 1998, pp. 1109–1112.
[16] S. D. Kee, I. Aoki, A. Hajimiri, and D. Rutledge, "The class-E/F family of ZVS switching amplifiers," *IEEE Trans. Microw. Theory Tech.*, vol. 51, no. 6, pp. 1677–1690, Jun. 2003.
[17] M. S. Alavi, R. B. Staszewski, L. C. N. de Vreede, A. Visweswaran, and J. R. Long, "All-digital RF I/Q modulator," *IEEE Trans. Microw. Theory Techn.*, vol. 60, no. 11, pp. 3513–3526, Nov. 2012.
[18] A. Mirzaei and H. Darabi, "Pulling mitigation in wireless transmitters," *IEEE J. Solid-State Circuits.*, vol. 49, no. 9, pp. 1958–1970, Sep. 2014.
[19] I. Bashir, R. B. Staszewski, O. Eliezer, B. Banerjee, and P. T. Balsara, "A novel approach for mitigation of RF oscillator pulling in a polar transmitter," *IEEE J. Solid-State Circuits*, vol. 46, no. 2, pp. 403–415, Feb. 2011.
[20] B. Razavi, "A study of injection locking and pulling in oscillators," *IEEE J. Solid-State Circuits*, vol. 39, no. 9, pp. 1415–1424, Sep. 2004.
[21] J. Mehta *et al.*, "A 0.8 mm^2 all-digital SAW-less polar transmitter in 65 nm EDGE SoC," in *IEEE Int. Solid-State Circuits Conf. (ISSCC) Dig. Tech. Papers*, Feb. 2010, pp. 58–59.

Kai Xu (S'16) was born in Dongying, China. He received the B.Sc. degree (*summa cum laude*) in electronics engineering from Shandong Normal University, Jinan, China, in 2012, and the M.Sc. degree in electronics engineering from Peking University, Beijing, China, in 2015. He is currently pursuing the Ph.D. degree with University College Dublin, Dublin, Ireland.

From 2013 to 2014, he was an Exchange Student with IMEC/INTEC Design Group (now IDLab), Ghent University, Ghent, Belgium. He was a Visiting Scholar with the John A. Paulson School of Engineering and Applied Sciences, Harvard University, Cambridge, MA, USA, in 2015. From 2017 to 2018, he was a Visiting Research Assistant with the State Key Laboratory of Analog and Mixed-Signal Very Large Scale Integration (VLSI), University of Macau, Macau, China. He held an Industry Internship with Beijing BLX IC Design Corporation, Beijing, in 2017. His research interests include ULP RF integrated circuits and systems for wireless communications.

Mr. Xu was a recipient of the National Scholarship in 2010, the Shandong Province Outstanding Graduate Student Award in 2012, the DUO-Belgium/Flanders Fellowship in 2013, and the 2018 IEEE SSCS Student Travel Grant Award. He serves as a reviewer for the IEEE JOURNAL OF SOLID-STATE CIRCUITS.

Feng-Wei Kuo was born in Kaohsiung, Taiwan, in 1976. He received the M.S. degree in electronics engineering form National Chiao Tung University, Hsinchu, Taiwan, in 2007. He is currently pursuing the Ph.D. degree with University College Dublin, Dublin, Ireland.

In 2007, he joined the Design Technology Division, Taiwan Semiconductor Manufacturing Company (TSMC), Hsinchu. He has authored or co-authored more than 13 technical papers. He holds 65 granted patents. His research interests include ultralow power transceiver and digital/analog phase-locked loops (PLLs), delay-locked loops, high-speed data-communication circuits design using advanced CMOS technology, and CMOS analog circuits.

Huan-Neng Ron Chen was born in Taichung, Taiwan, in 1982. He received the B.S. degree in electrical engineering from National Sun Yat-sen University, Kaohsiung, Taiwan, in 2004, and the M.S. degree in electronics engineering from National Chiao Tung University, Hsinchu, Taiwan, in 2006.

He is involved in the development of RF transceiver. In 2007, he joined the Design and Technology Platform of Taiwan Semiconductor Manufacturing Company (TSMC), Hsinchu, where he has worked on RF design and all-digital phase locked loop for next-generation wireless/wireline applications.

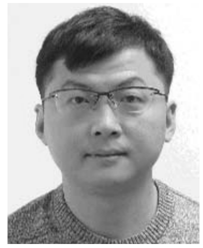

Lan-Chou Cho was born in Taipei, Taiwan, in 1978. He received the B.S., M.S., and Ph.D. degrees in electrical engineering from National Taiwan University, Taipei, Taiwan, in 2001, 2003, and 2008, respectively.

From 2009 to 2014, he was with Mediatek Inc., Hsinchu, Taiwan. He is currently with Taiwan Semiconductor Manufacturing Company (TSMC), Inc., Hsinchu. His research interests include phase-locked loops, and high-speed CMOS data-communication circuits for silicon photonic applications.

Chewn-Pu Jou received the B.S.E.E. and M.S.E.E. degrees from National Taiwan University, Taipei, Taiwan, in 1982 and 1984, respectively, and the Ph.D. degree from the State University of New York, Stony Brook, NY, USA, in 1991.

He was an RF designer for wireless LAN circuits and low temperature co-fired ceramic components with the Industrial Technology Research Institute, Hsinchu, Taiwan. In 1998, he initiated RFCMOS technology development at United Microelectronics Corporation, Hsinchu. In 2001, he started Uwave tech. delivering RFCMOS wireless devices. Since 2006, he has been leading the Taiwan Semiconductor Manufacturing Company, Hsinchu, RF design team to help RF foundry business.

Dr. Jou was a recipient of the National Award of the 1997 Best MOEA Program.

Mark Chen, photograph and biography not available at the time of publication.

Robert Bogdan Staszewski (M'97–SM'05–F'09) was born in Bialystok, Poland. He received the B.Sc. (*summa cum laude*), M.Sc., and Ph.D. degrees in electrical engineering from the University of Texas at Dallas, Richardson, TX, USA, in 1991, 1992, and 2002, respectively.

From 1991 to 1995, he was with Alcatel Network Systems, Richardson, TX, USA, where he was involved in sychronous optical networking cross-connect systems for fiber optics communications. In 1995, he joined Texas Instruments Incorporated, Dallas, TX, USA, where he was elected as a Distinguished Member of Technical Staff (limited to 2% of technical staff). From 1995 to 1999, he was engaged in advanced CMOS read channel development for hard disk drives. In 1999, he co-started the Digital RF Processor (DRP) Group within Texas Instruments, Dallas, TX, USA, with a mission to invent new digitally intensive approaches to traditional RF functions for integrated radios in deeply scaled CMOS technology. He was appointed as a Chief Technology Officer of the DRP Group from 2007 to 2009. In 2009, he joined the Delft University of Technology, Delft, The Netherlands, where he currently holds a guest appointment of a Full Professor (*Antoni van Leeuwenhoek Hoogleraar*). Since 2014, he has been a Full Professor with the University College Dublin (UCD), Dublin, Ireland. He has authored or co-authored four books, five book chapters, 260 journal and conference publications. He holds 180 issued U.S. patents. His research interests include nanoscale CMOS architectures and circuits for frequency synthesizers, and transmitters and receivers.

Dr. Staszewski is a TPC Member of ISSCC, RFIC, ESSCIRC, ISCAS, and RFIT. He is an upcoming TPC Chair of 2019 ESSCIRC, Krakow, Poland. He was a recipient of the 2012 IEEE Circuits and Systems Industrial Pioneer Award.